NWP Ocean Calibration for the CFOSAT wind scatterometer and wind retrieval evaluation

Zhen Li[1], Ad Stoffelen[2], Anton Verhoef[3], and Jeroen Verspeek[4]

[1, 2, 3, 4]Royal Netherlands Meteorological Institute.

Corresponding author: Zhen Li (li@knmi.nl)

Abstract

The unique rotating fan-beam feature of SCAT onboard CFOSAT leads to varying geometries across the swath and furthermore leads to varying wind retrieval performance across the swath. The Wind Vector Cells (WVCs) across the swath are classified into outer, sweet and nadir. The sweet WVCs contain the most diverse geometries, which lead to the best wind retrieval performance. In the outer WVCs the azimuth and incidence angle diversity is very limited and the number of views is smallest, which makes the wind retrieval the most ambiguous and difficult to improve. Secondly, in order to improve the wind retrieval, two kinds of NWP Ocean Calibration (NOC) are applied. One is a NOC as a function of incidence angle (NOCinc). The other one is a newly developed NOC as a function of incidence angle and antenna azimuth angle (NOCant), which takes the rotation angle into account. The NOCant correction results in better fits of the Geophysical Model Function than the NOCinc correction does, except for the outer WVCs, where the limited diversity of views determines retrieval quality. The results show that NOCant correction improves the wind speed Probability Distribution Function per WVC and reduces the average wind direction bias and the relative wind direction (relative to the satellite motion direction) biases, as compared to NOCinc correction. In conclusion, the rotating fan-beam feature of SCAT leads to unique and various data characteristics across the swath. Overall the performance of the proposed NOCant correction is better than NOCinc and improves the wind statistics.

1 Introduction

The Chinese-French Oceanography Satellite (CFOSAT) was launched on 29 October 2018 (00:43 UTC). The goal of this joint mission is to monitor the ocean surface winds and waves in order to provide data on related ocean and atmospheric applications. The wind scatterometer, briefly called SCAT, onboard of CFOSAT is the first Rotating Fan-beam Scatterometer (RFSCAT). There are three types of scatterometer in orbit: multiple fixed fan-beam ASCAT-A/B/C, rotating pencil-beam SCATSat-1, HY-2A/B/C) and rotating fan-beam (SCAT). ASCAT on the European Organization for the Exploitation of Meteorological Satellites (EUMETSAT) Metop satellite series has six C-band VV polarized fan beams. There are three beams pointing to the left of the satellite ground track and three beams pointing to the right, which gives three independent views per Wind Vector Cell (WVC) (Gelsthorpe, Schied, and Wilson 2000). SCATSat-1 was launched by the Indian Space Research Organization (ISRO) in 2016 as a Ku-band rotating pencil-beam scatterometer as a replacement of OSCAT on Oceansat-2. The HY-2 satellites are launched by the Chinese National Satellite Ocean Application Service (NSOAS) and carry Ku-band rotating pencil-beam scatterometers. Rotating pencil-beam scatterometers can derive four independent views (two VV and two HH polarization) per WVC in the inner swath, and only two independent views (VV) per WVC in the outer swath, which latter leads to increased wind direction ambiguity. The SCAT on CFOSAT is the only rotating fan-beam scatterometer in orbit and like pencil-beam scatterometers it provides multiple views in Ku-band VV and HH polarization per WVC, with a geometry dependent on the location across the swath. It combines the features of fixed fan-beam and rotating pencil-beam ((Lin et al. 2000; Li, Stoffelen, and Verhoef 2019)) and it is able to provide large swath coverage and also increases the diversity of the geometries intensively compared to the other two scatterometer types in part of the swath.

1.1 SCAT characteristics

The slowly rotating fan beam of SCAT sweeps over the swath and results in multiple overlapping views in each individual WVC. The elongated surface footprint is cut into so-called slices, providing different geometrical views in each WVC. The number of views in a WVC depends on its location in the swath and on the rotation speed of the fan beam. The WVCs located at outer and nadir swath contain a smaller number of views and less azimuth diversity due to the scanning geometry, which leads to a degraded wind retrieval performance. On the contrary, the scanning geometry leads a diverse geometry and more views in the other parts of the swath (named sweet swath), which results in a better wind retrieval performance as compared to nadir and outer swath. The main parameters of SCAT are shown in Table 1. SCAT level-1B (L1B) data have been simulated and tested in (Li, Stoffelen, and Verhoef 2019). The geometry distribution of the real L1B data is in line with the simulated data with minor differences (Figure 1). Figure 2 (a) shows the circular motion of the slices in the real L1B data and (b) shows the simulated L1B data. Both datasets show the scanning geometry features mentioned above (diverse geometry and more overlapping at sweet swath and limited geometry and a smaller number of slices at nadir and outer swath). For real data, the data dimension is 40×75×12,480, which implies that each pulse has 40 slices, every 75 pulses are grouped into one frame, and there are 12,480 frames per orbit. The location of the slices with the same slice number (Figure 1, e.g. number 40) per 75 pulses are not connected as a smooth line, becausethe cutting of the slices in each frame varies, which leads to varying incidence angles for the same slice number (Figure 1 a).

Table 1. Main parameters of CFOSAT SCAT (Li, Stoffelen, and Verhoef 2019)

Parameters	**Value**
Orbit height	514 km
Swath	1000 km
Footprint	280 km
Satellite speed	7.1 km/s
Antenna rotating speed	3.5 rpm
Polarization	VV and HH alternating
Incidence angle range	25 – 48 deg
Antenna pointing angle	40 deg
Peak transmit power	120 W
WVC resolution	25 km
Center frequency	13.256 GHz (Ku-band)
Duration of transmit pulse	1.3 ms
Duration of receiving pulse	2.7 ms
Pulse Repetition Frequency (PRF)	75 Hz
Two-way -3dB beam width (azimuth)	1.28 deg
Peak antenna gain	30 dB
Transmit bandwidth	0.5 MHz

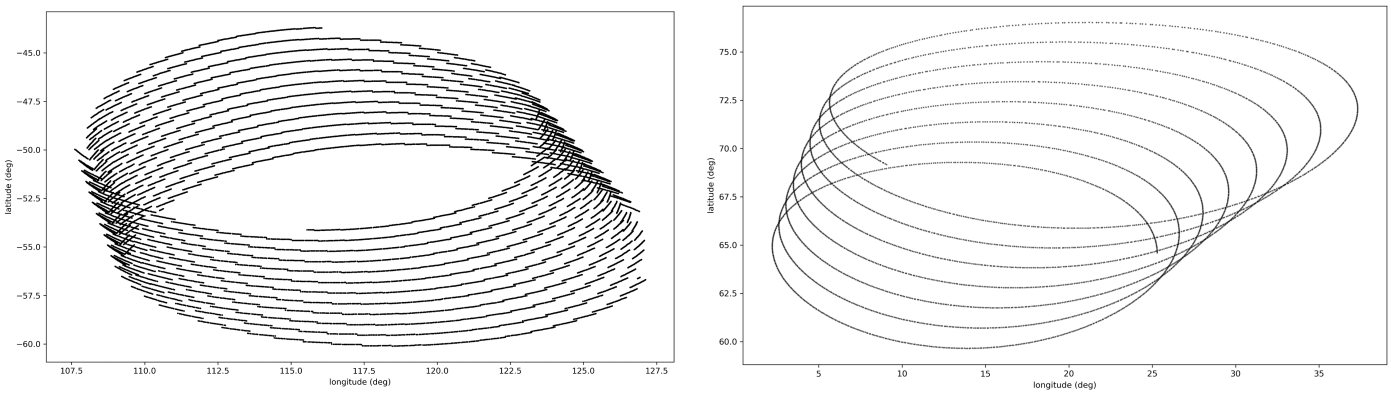

(a) (b)

Figure 1. (a) SCAT level-1B data: slice (number 40, located at the end of each pulse) location of one orbit. (b) Simulated level-1B data: slice (number 40, located at the end of each pulse) location of one orbit.

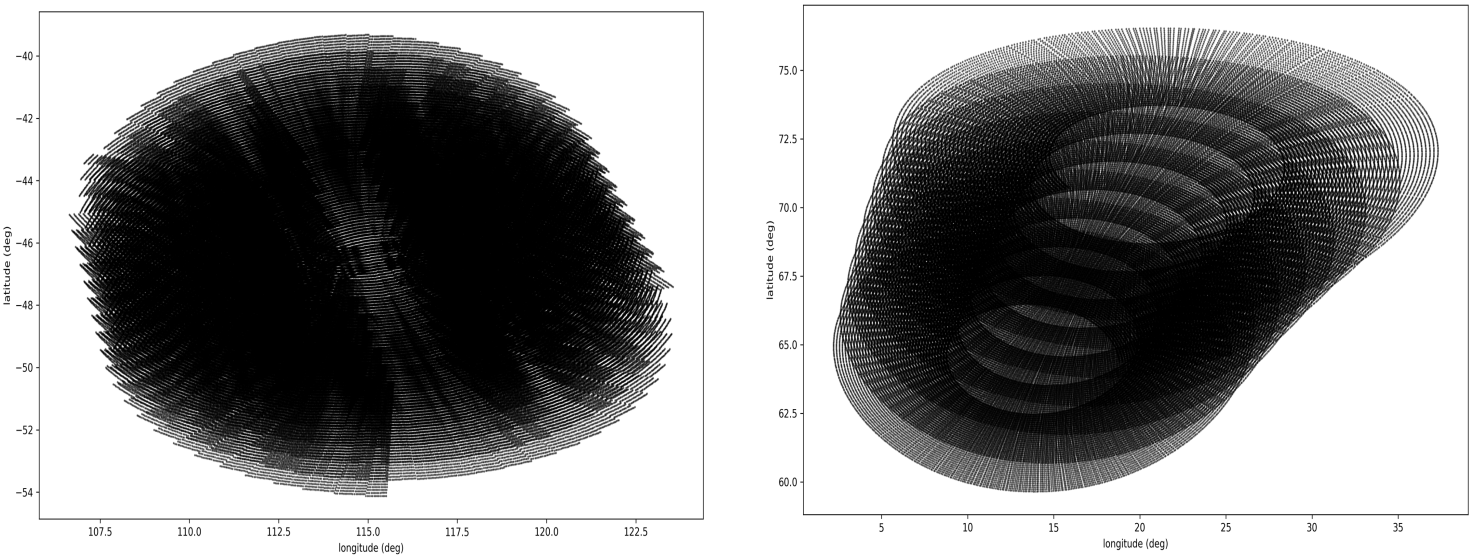

(a) (b)

Figure 2. The circular motion of the slices in comparison with simulated data: (a) real data. (b) simulated data.

1.2 NWP Ocean Calibration

To obtain standard backscatter calibration for scatterometers it is essential to use backscatter corrections. These corrections are needed to obtain standard quality of the wind products. The NWP (Numerical Weather Prediction) Ocean Calibration (NOC) is designed to find absolute corrections of measured backscatter $\sigma°$, such the mean value matches simulated $\sigma°$ by the Geophysical Model Function (GMF) using input NWP model winds (Stoffelen and Anderson 1997)(Freilich, Qi, and Dunbar 1999). This method has been successfully implemented for the ERS scatterometers (Stofflen 1999), ASCAT (Verspeek et al. 2012), and pencil-beam scatterometers (Yun et al. 2012). In this paper, NOC as a function of incidence angle (NOCinc) and a newly developed NOC using corrections as a function of incidence angle and antenna azimuth angle (NOCant) are applied. The latter considers the rotation of SCAT by including antenna azimuth angle into the correction.

The aim of our study is to analyze and understand the characteristics of the SCAT data, evaluate the proposed NOCant and NOCinc method and the associated wind retrieval performance.

2. Characteristics of level-2A data

The wind retrieval process consists of two main parts (Figure 3): (1) assign the L1B backscatter slices to the proper WVCs and aggregate the L1B slices of the same geometry in a WVC into views (L2A data); (2) wind retrieval using the aggregated views with maximum likelihood estimation (MLE).

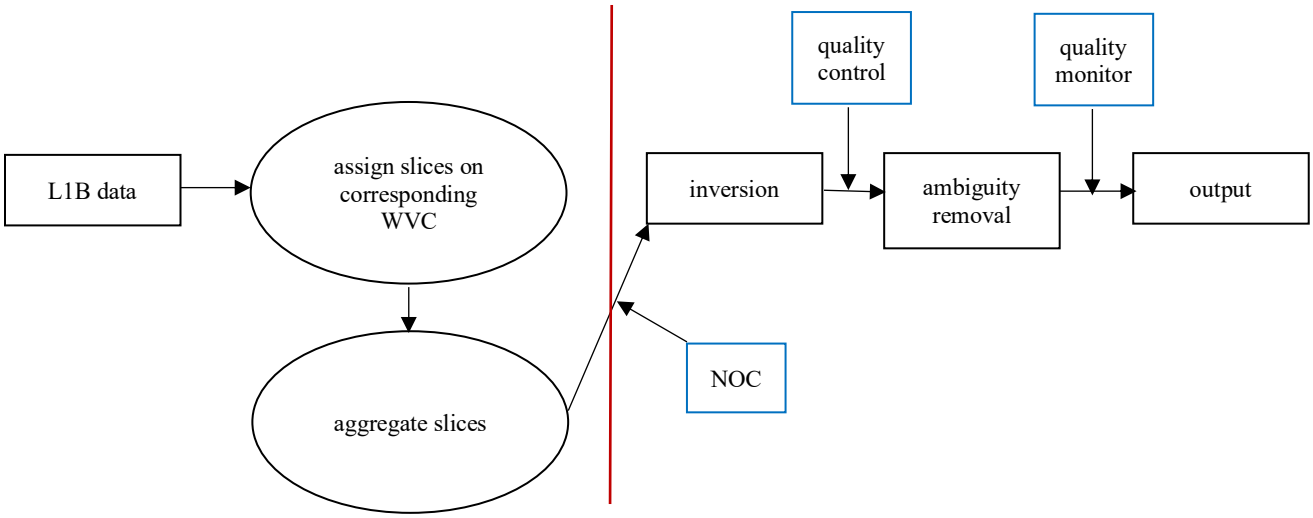

Figure 3. The workflow of wind retrieval process.

L1B data are assigned to the corresponding WVCs by setting up a sub-track swath coordinate for the slices. A sub-track grid is set up in along-track and cross-track directions with Wind Vector Cells (WVCs) of about 25km x 25km or 50km x 50km (Figure 4). The geographic positions of the slices are converted to the sub-track grid Cartesian coordinate by Space Oblique Mercator (SOM) projection (Dunbar et al. 2001)(Snyder 1982). In the new coordinate system,

the slice positions are assigned to the specific WVCs and the slices belonging to the same WVC with the same antenna revolution and polarization are aggregated into one view.

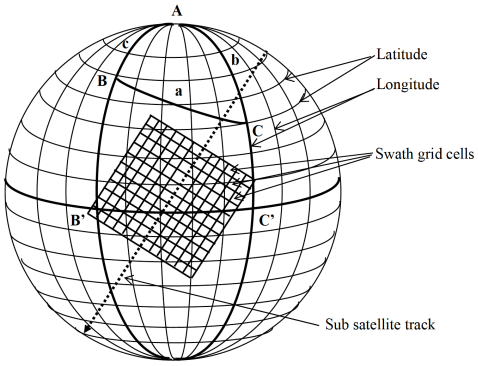

Figure 4. Satellite sub-track grid (SCAT-DP team 2010).

Figure 5 (a) and (b) indicate that the slices are correctly located on the converted sub-track coordinates and assigned to the corresponding WVCs. The distribution of the slices in each WVC is varying depending on the across track location (Figure 5 (c)). The WVCs can be classified into three groups: outer WVCs (number 1-5, number 38-42); sweet WVCs (number 6-12, number 31-37); nadir WVCs (number 13-30). The sweet WVCs contain the largest number of slices compared to the nadir and outer WVCs and the slice position pattern at the sweet WVCs is rather mixed because these WVCs have the most diverse azimuth distribution. At nadir azimuth views are limited to a repeatable pattern depending on WVC . The slices in the outer WVCs are more diverse, because the number of slices and the number of views are both the smallest and somewhat depending on latitude due to earth and orbit characteristics.

Figure 6 shows the azimuth (antenna direction relative to the sub-track direction) distribution as a function of WVC, which shows that the azimuth is around 0°/360° or 180° at the nadir WVCs, around 90° and 270° at the outer WVCs and quite diverse at the sweet WVCs. Even though the azimuth diversity is limited at the nadir swath, it contains the large range of incidence angles, while only high incidence angles fall in the outer WVCs (Figure 7). The number of views as a function of WVC is shown in Figure 8. This distribution has a saddle shape with the largest number of views in the sweet swath, conform (Li, Stoffelen, and Verhoef 2019).

The contoured histograms of measured σ° and simulated σ° (HH and VV polarization) are shown in Figure 9. The simulated σ° for a specific beam ('view') is computed using the collocated ECMWF model stress-equivalent wind (De Kloe, Stoffelen, and Verhoef 2017), the beam geometry (azimuth and incidence angles), and the Geophysical Model Function (NSCAT4-DS) (Wang et al. 2017). A deviation from the diagonal occurs in the HH σ° histogram, while the deviation in the VV σ° histogram is rather small. The outer WVCs contribute most to the deviation (Figure 10). Figure 11 shows measured and simulated σ° Probability Density Functions (PDF) per incidence angle. The negative σ°s indicate the existence of very low winds in the presence of noise, where σ°s with low incidence angle contain the greatest number of negative σ°s, while the σ°s with medium incidence angle contain the smallest number of negative σ°s. VV polarized σ°s have more negative values than HH polarized σ°s. Even though σ° theoretically cannot be negative, because wind speed is always positive, negative σ°s still are valid due to measurement noise and section 3 explains how to make use of them.

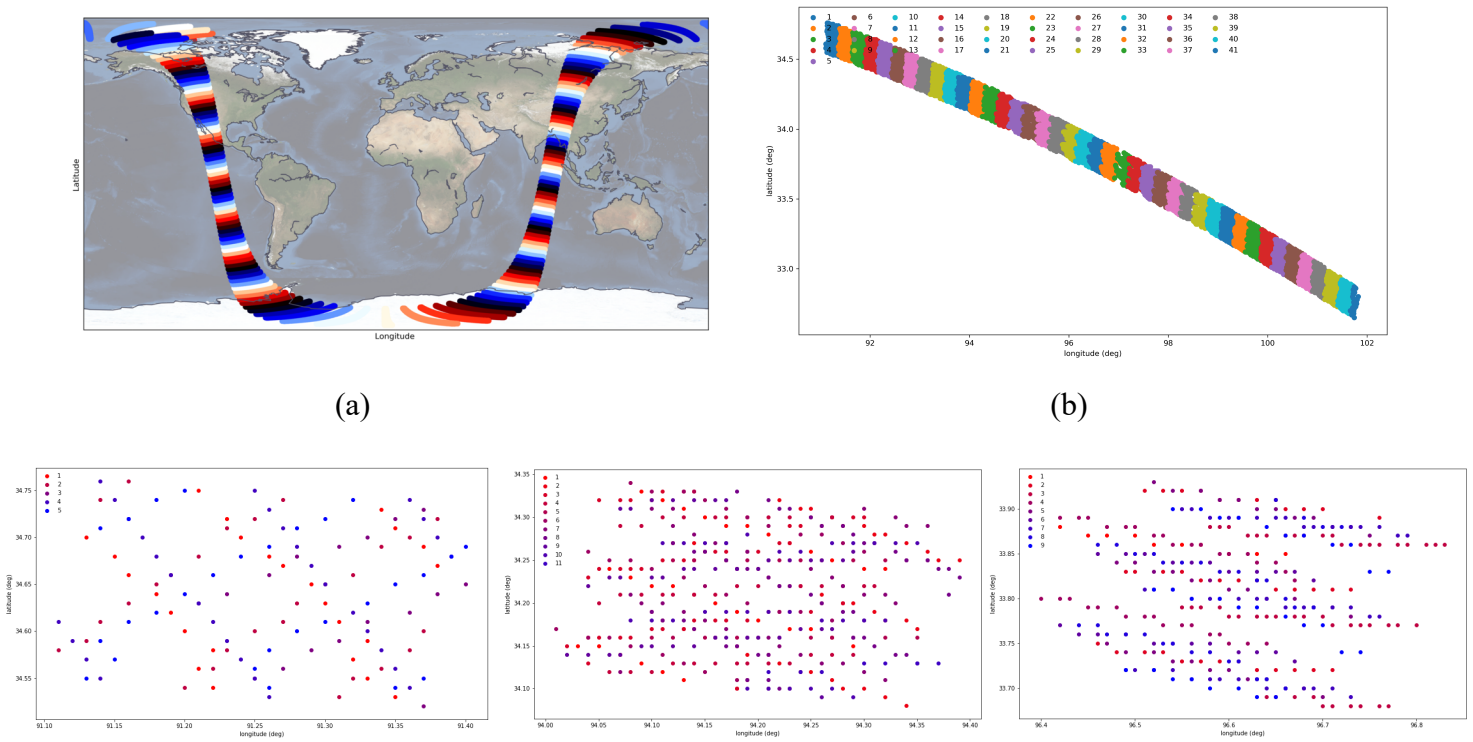

Figure 5. Orbit 20191103T004727_20191103T022120. (a) Illustration of the slices organized by rows (10 rows interval); (b) WVC distribution of the row number 300 (different colour indicates different WVCs); (c) Slice positions in the outer WVC number 2, sweet WVC number 11 and nadir WVC number 22 (from left to right), different colour indicates different view.

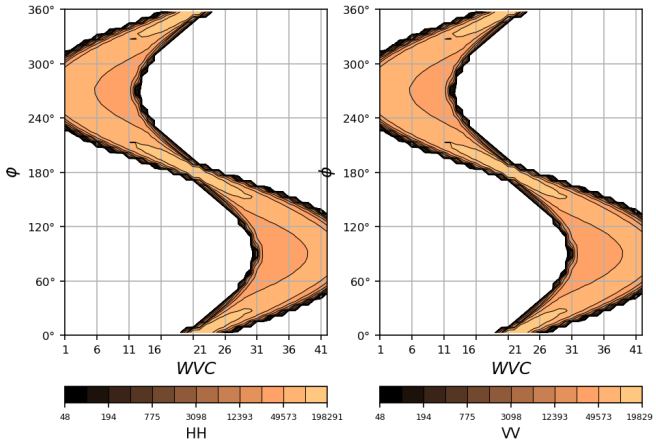

Figure 6. Azimuth angle (antenna direction relative to the satellite movement direction) distribution as a function of WVC number across the track.

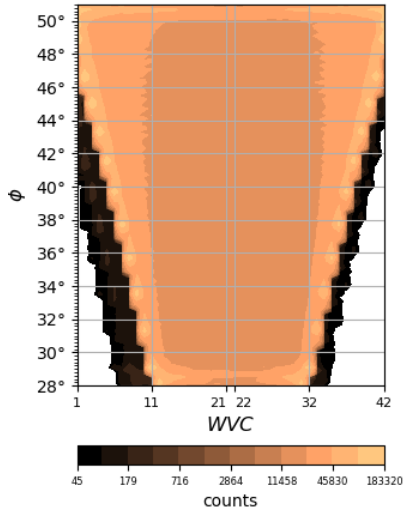

Figure 7. Incidence angle distribution as a function of WVC number across the track.

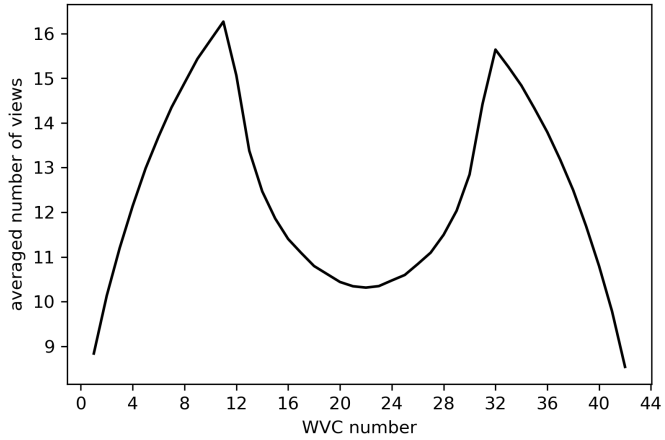

Figure 8. Average number of views at the WVCs across the swath.

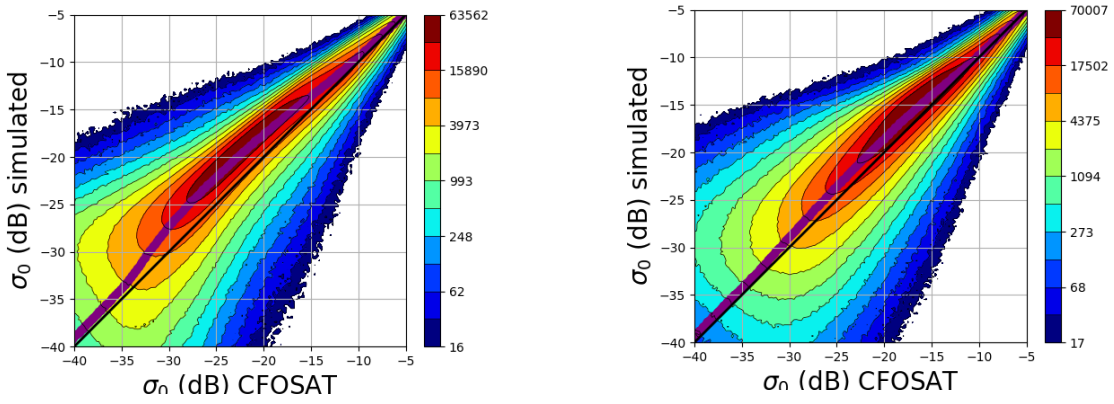

(a) (b)

Figure 9. Contoured histograms of the joint distribution of measured $\boldsymbol{\sigma}^\circ$ and simulated $\boldsymbol{\sigma}^\circ$. (a) HH polarization; (b) VV polarization. The purple line denotes the mean difference as a function average simulated and measured $\boldsymbol{\sigma}^\circ$.

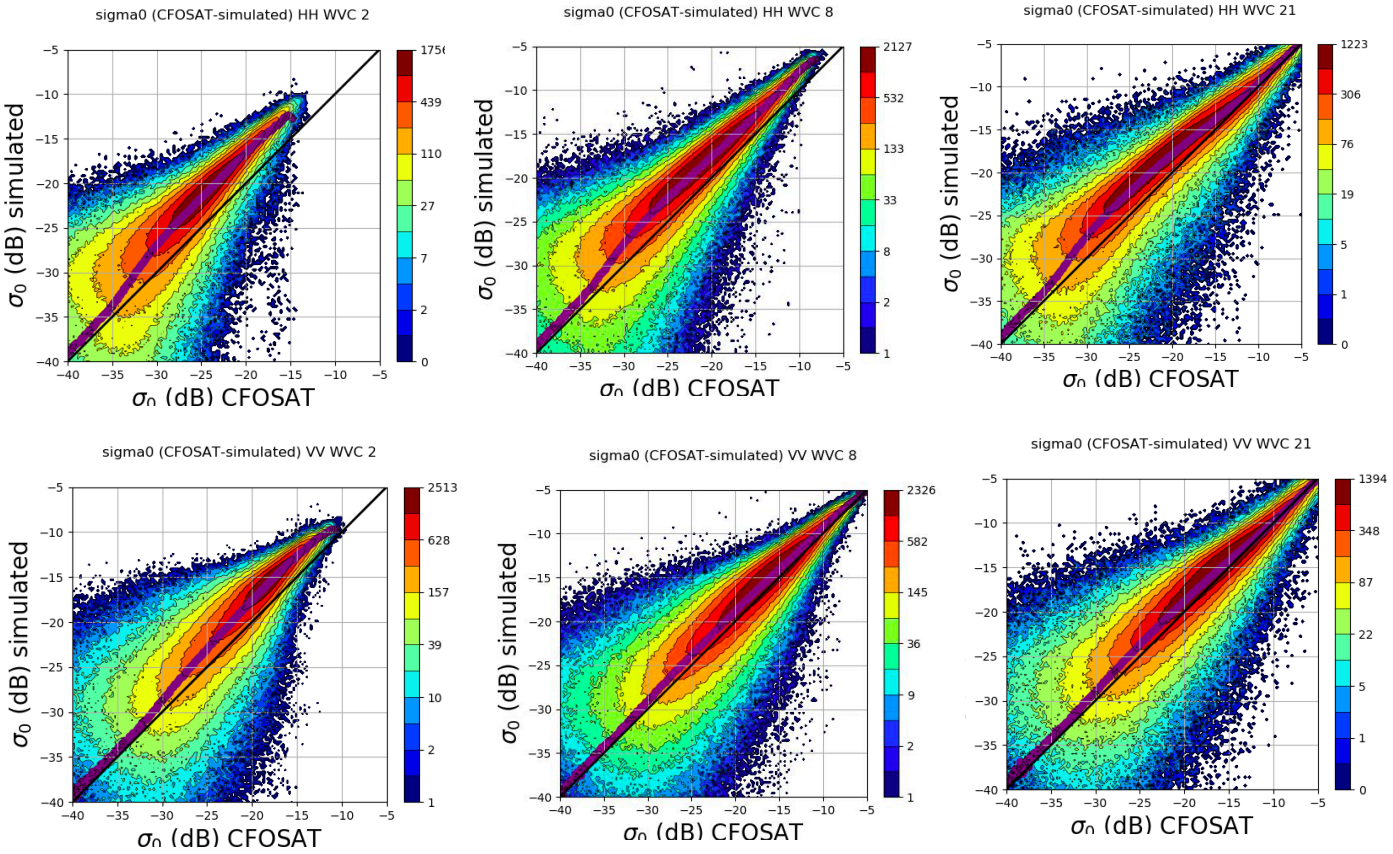

(a) (b) (c)

Figure 10. Contoured histograms of the joint distribution of measured $\boldsymbol{\sigma}^{\circ}$ and simulated $\boldsymbol{\sigma}^{\circ}$ at (a) the outer WVC (number 2), upper plot is HH, lower plot is VV; (b) sweet WVC (number 8), upper plot is HH, lower plot is VV; (c) nadir WVC (number 21), upper plot is HH, lower plot is VV. The purple line denotes the mean difference as a function of average simulated and measured $\boldsymbol{\sigma}^{\circ}$.

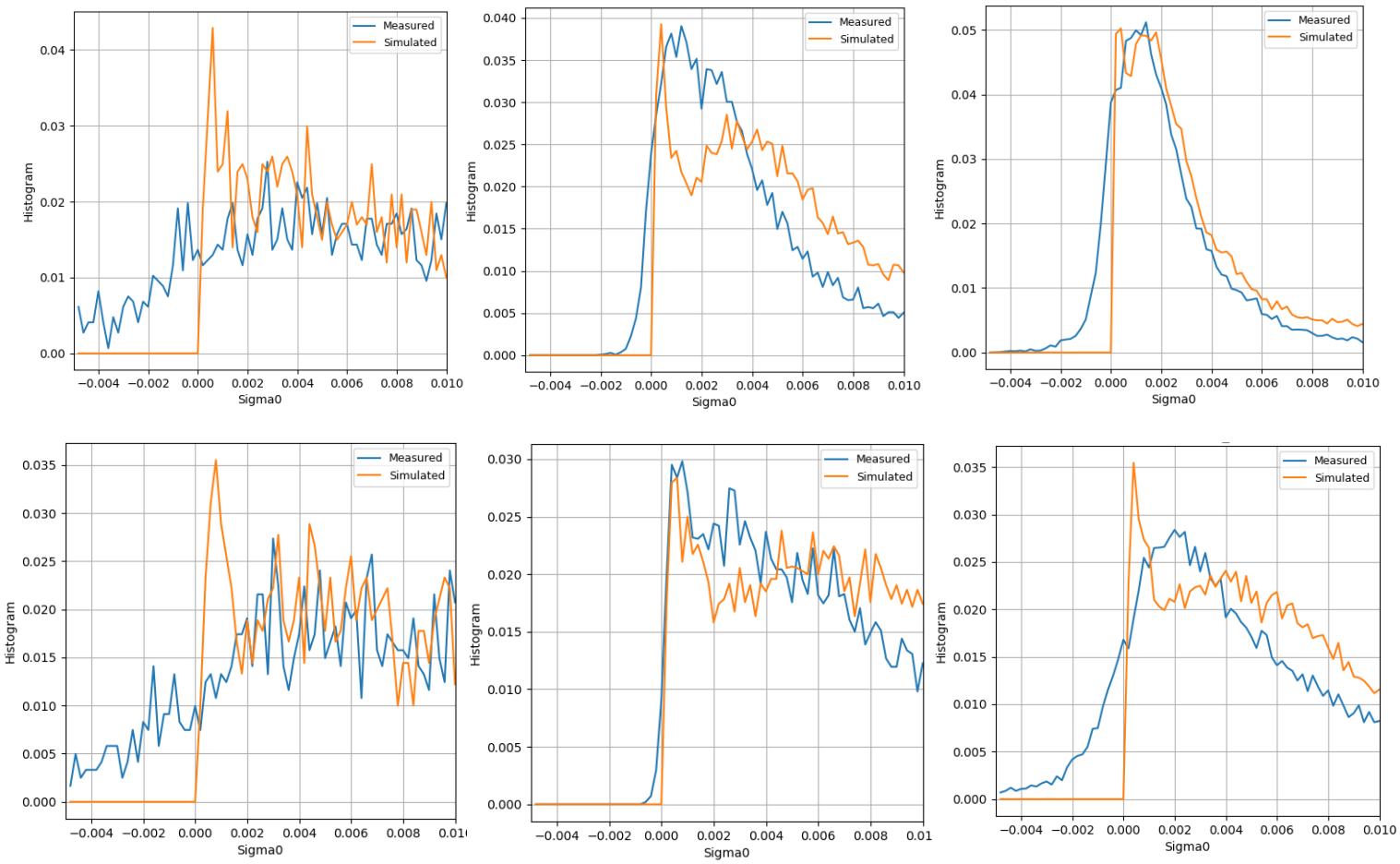

Figure 11. PDFs of measured $\boldsymbol{\sigma}^\circ$ and simulated $\boldsymbol{\sigma}^\circ$ for polarization HH (upper row) or VV (lower row). Column (a) $\boldsymbol{\sigma}^\circ$ PDF with incidence angle 30°; (b) $\boldsymbol{\sigma}^\circ$ PDF with incidence angle 42°; (c) $\boldsymbol{\sigma}^\circ$ PDF with incidence angle 50°.

3. Wind inversion method

The classic algorithm for wind retrieval is Maximum Likelihood Estimation (MLE), which has been applied in many studies ((Chi and Li 1988; Pierson 1989; M Portabella and Stoffelen 2002)). It is adopted here and can be written as:

$$MLE = \frac{1}{N}\sum_{i=1}^{N}\left(\frac{\sigma^\circ_{mi} - \sigma^\circ_{si}}{Kp(\sigma^\circ_{xi})}\right)^2 \tag{1}$$

where σ°_{mi} is measured σ°, σ°_{si} is trial simulated σ°. $Kp(\sigma^\circ_{xi})$ is the expected Gaussian observation noise with the form of $Kp \times \sigma^\circ_{xi}$. σ°_{xi} is usually taken to be either σ°_{mi} or σ°_{si}. N is the number of views. The inversion basically takes a set of views (σ°_{mi} together with their geometries) in one WVC and searches for the σ°_{si} through a GMF by varying wind speed and

wind direction to find the minimum MLE. However, the found minimum solution is not always the best solution due to the ambiguity, so Two-Dimensional Variational Ambiguity Removal (2DVAR) (Vogelzang 2013) together with Multiple Solution Scheme (MSS) (Marcos Portabella and Stoffelen 2004)(Vogelzang and Stoffelen 2018) are applied to do the selection in combination with both observational and NWP background contributions.

Many negative σ°s (Figure 11) are observed. Negative σ°s arise since a noise measurement N is subtracted from the received signal power values P: $\sigma^\circ = P - N$. In case of a low backscatter value the result of the subtraction can be negative, due to the errors δ : $\delta\sigma^\circ = \delta P + \delta N$, . SCAT gives $\sigma^\circ + \delta\sigma^\circ < 0$ at low winds as shown in Figure 11. However, the GMF cannot simulate negative σ° since the wind speed is always positive. Nevertheless, the negative σ°s still are valid and contribute to the retrieval of the low winds. In order to make use of them, an extra term $-2ln(v)$ is added to (1):

$$MLE = \frac{1}{N}\sum_{i=1}^{N}\left(\frac{{\sigma^\circ}_{mi} - {\sigma^\circ}_{si}}{Kp({\sigma^\circ}_{xi})}\right)^2 - 2ln(v) \tag{2}$$

where v is wind speed and it has been successfully implemented in the PenWP (Pencil-beam Wind Processor) code (Verhoef n.d.). Equation (2) follows from Bayesian estimation using prior knownledge $v \in [0, \infty)$, such that probability $Prob(v < 0) = 0$, $Prob(v > 0) \neq 0$ and for low winds $P(v) \propto v$. The logarithmic term contributes strongly to the MLE when the wind speed approaches to zero and thus penalizes the cost function.

3.1 NWP Ocean Calibration

The NWP Ocean Calibration (NOC) (Stofflen 1999)(Verspeek et al. 2012) is used to assess the difference between the scatterometer backscatter data and the simulated backscatter data from collocated NWP winds using the GMF. This is needed since there is no accurate absolute radar calibration and the scatterometer standard wind processing needs a calibration standard. NOC provides a relative intercalibration standard for given GMF and given calibrated global input stress-equivalent vector winds. The objective of NWP Ocean Calibration (NOC) is to find corrections of the normalized radar cross section σ° in order to obtain standard wind retrieval quality, and the corrections are indicated as NOC residuals. The simulated backscatter is given by the GMF (Wentz, Peteherych, and Tomas 1984) (Wentx and Smith 1999):

$$\sigma^\circ(\theta, v, \phi) = A_o(v, \theta)(1 + A_1(v, \theta)cos\phi + A_2(v, \theta)\cos(2\phi)) \tag{3}$$

where θ is the incidence angle, v is the wind speed, and ϕ is the relative wind direction with respect to the antenna pointing direction. The A coefficients only depend on the wind speed and the incidence angle. The mean backscatter is determined by the value of A_o ideally without contributions from A_1 and A_2, even though the contributions cannot be excluded completely, we try to minimize their contribution. Integrating uniformly over the azimuth angle:

$$\frac{1}{2\pi}\int_0^{2\pi} \sigma^\circ(\theta, v, \phi)\, d\phi = A_o(v, \theta) \tag{4}$$

So if 1) the true WVC wind direction is sampled uniformly for all wind speeds and incidence angles, 2) the WVC wind speed and 3) A_o are perfectly known, then the mean of $A_o(v,\theta)$ is identical to the mean of $\sigma°$, which implies that the uncertainties in $A_1(v,\theta)$ and $A_2(v,\theta)$ have no contribution to the simulated mean $\sigma°$. Note that in practice instrument intercalibration implies that the sum of the errors of the input wind vector, GMF and the NOC procedure are taken identical for the different instruments. Figure 12 gives the description of the calculation scheme of the mean $\sigma°$. $\langle\sigma°\rangle$ represents the mean backscatter value over a uniform wind direction distribution for measured ${\sigma°}_{mk}$ or simulated ${\sigma°}_{sk}$ by collocated NWP wind inputs through the GMF. In order to derive a uniform wind direction distribution, the data are split into wind speed bins (1m/s, from 0-30m/s) and azimuth bins (12° bin, from 0-360°, NWP wind direction relative to the antenna azimuth angle). The average $\sigma°$ over the total number of measurements is taken at each wind direction bin and subsequently averaged over wind speed. Each value in a wind speed bin is multiplied by the number of measurements in that bin, which value is averaged and normalized over all speed bins to obtain the average simulated backscatter value. Bins are defined as large enough to have a minimum number of measurements and small enough to provide a good approximation of the integral. The difference between the mean measured $\sigma°$ and the mean simulated $\sigma°$ is used as correction factor for the instrument.

The classical way to calculate the NOC is to take NOC as a function of incidence angle (referred as NOCinc), which has proven to be effective for fixed fan-beam scatterometers, while for rotating pencil-beam instruments a VV and HH calibration is computed as their measurements are each made at fixed incidence angle (Verspeek et al. 2012)(Yun et al. 2012). SCAT has a unique rotating fan-beam antenna, which shows an azimuth-dependent $\sigma°$ gain variation. We therefore developed an NOC as a function of both incidence angle and antenna azimuth angle (referred to as NOCant) in order to take the rotation angle into account. Both methods are applied and analyzed in section 4.

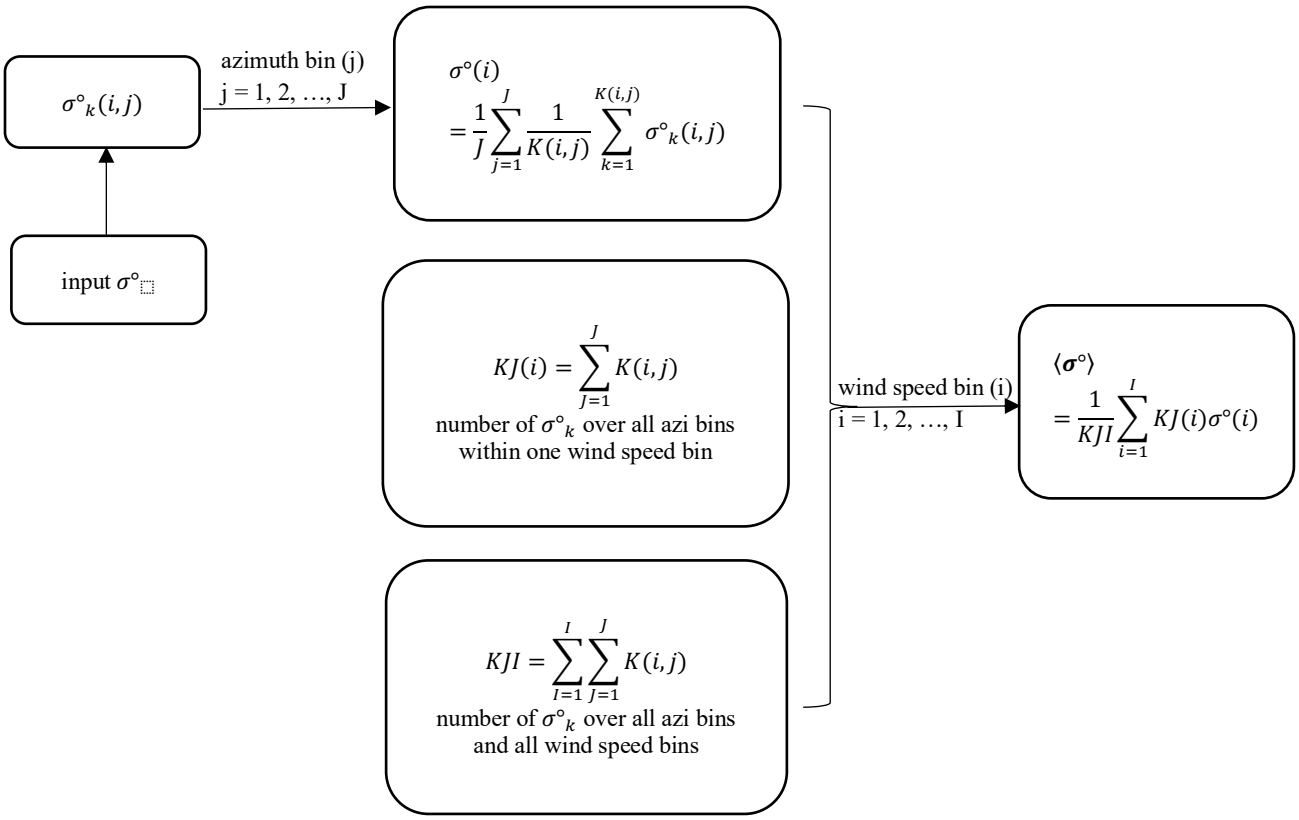

Figure 12. Calculation scheme of the mean $\langle\boldsymbol{\sigma}^\circ\rangle$, (i – wind speed bin; I – total number of bins of wind speed; j – azimuth angle bin; J – total number of bins of azimuth angle; k – index of individual measurement at the bin of (wind speed bin, azimuth bin) $\sigma^\circ_k(i,j)$; K – total number of measurement at the bin of (wind speed bin, azimuth bin) K(i, j).

3.1.1 NOC as a function of incidence angle

σ°s are binned into the incidence angle bins (bin size 1°, angle range ∈ [28°, 51°)) and they are the input in Figure 12 to derive the mean σ° for both measured and simulated σ°. Figure 13 shows the calculated NOCinc for HH and VV polarization. The x axis indicates the incidence angle bin, e.g., 30° represents the correction value calculated from the incidence angle interval from 30° to 31°, so the σ°s with incidence angle in between 30° and 31° are corrected with the value corresponding to incidence angle bin 30 in Figure 13. The value of the HH correction decreases as a function of incidence angle, except that it increases at the high incidence angle bins with quite a large jump at 50°. The value of the VV correction increases a bit at the low incidence angle and then shows a similar pattern to the HH correction with also a large jump at 50°.

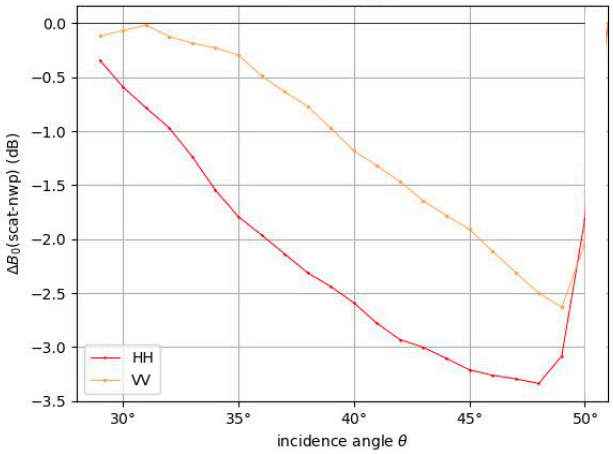

Figure 13. NOC as a function of incidence angle for 25km product for 2019.

3.1.2 NOC as a function of incidence angle and antenna azimuth angle

σ°s are first binned into antenna azimuth angle bins (bin size 10°, [0 to 360°)) and then in each antenna azimuth angle bin, the σ°s are binned into incidence angle bins (bin size 1°, [28° to 50°)). They are the input in Figure 12 to derive the mean σ° for both measured and simulated σ°. Figure 14a shows the NOCant as a function of incidence angle per antenna azimuth angle bin and Figure 14b shows the NOCant as a function of antenna azimuth angle per incidence angle bin. In order to apply the correction, the antenna azimuth angle of a σ° is checked first to find out which antenna azimuth bin it falls in and then the incidence angle bin is decided as well. Then the correction value is found for the σ°.

The NOCant curves in Figure 14a show the same shape as NOCinc in Figure 13, but with a vertical spread of about 0.2dB. Ideally the NOCant of the same incidence angle at different antenna azimuth angles should have the same value, which means that the lines in Figure 14b should be flat. However, there are significant oscillations around the antenna azimuth angle at 90°, 100°, 270°, and 280°, especially at the high incidence angle of 50°. This might be caused by the changing sign of the frequency modulation for forward and backward looks and a low number of samples in the level 0 data processing, which is inevitable. There are less than five samples per incidence angle and per polarization at those antenna azimuth angles. Data for one month with 446 orbits are applied here, and the azimuth variations do not disappear by further increasing the amount of input data (not shown). In order to avoid the large oscillation, NOCant is extrapolated at the incidence angle 50° , where the antenna azimuth angles are 90°, 100°, 270°, and 280° (Figure 15 a and b). Moreover, the NOCant is not as smooth as the NOCinc due to the binning and the limitation of the number of samples in each antenna azimuth angle bin and incidence bin. A 3rd order polynomial fit function is applied on the extrapolated NOCant (Figure 15 c and d) in order to have smoother lines.

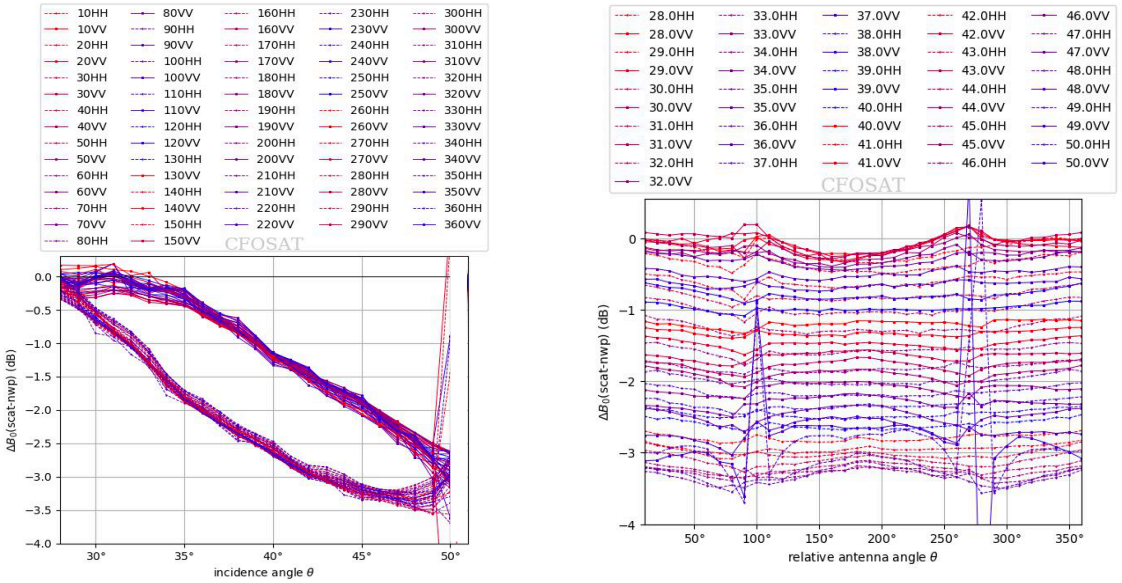

(a) (b)

Figure 14. (a) NOCant for the 25-km product as a function of incidence angle per antenna azimuth angle bin; (b) NOCant as a function of antenna azimuth angle per incidence angle bin. Dashed lines are HH polarization, solid lines are VV polarization.

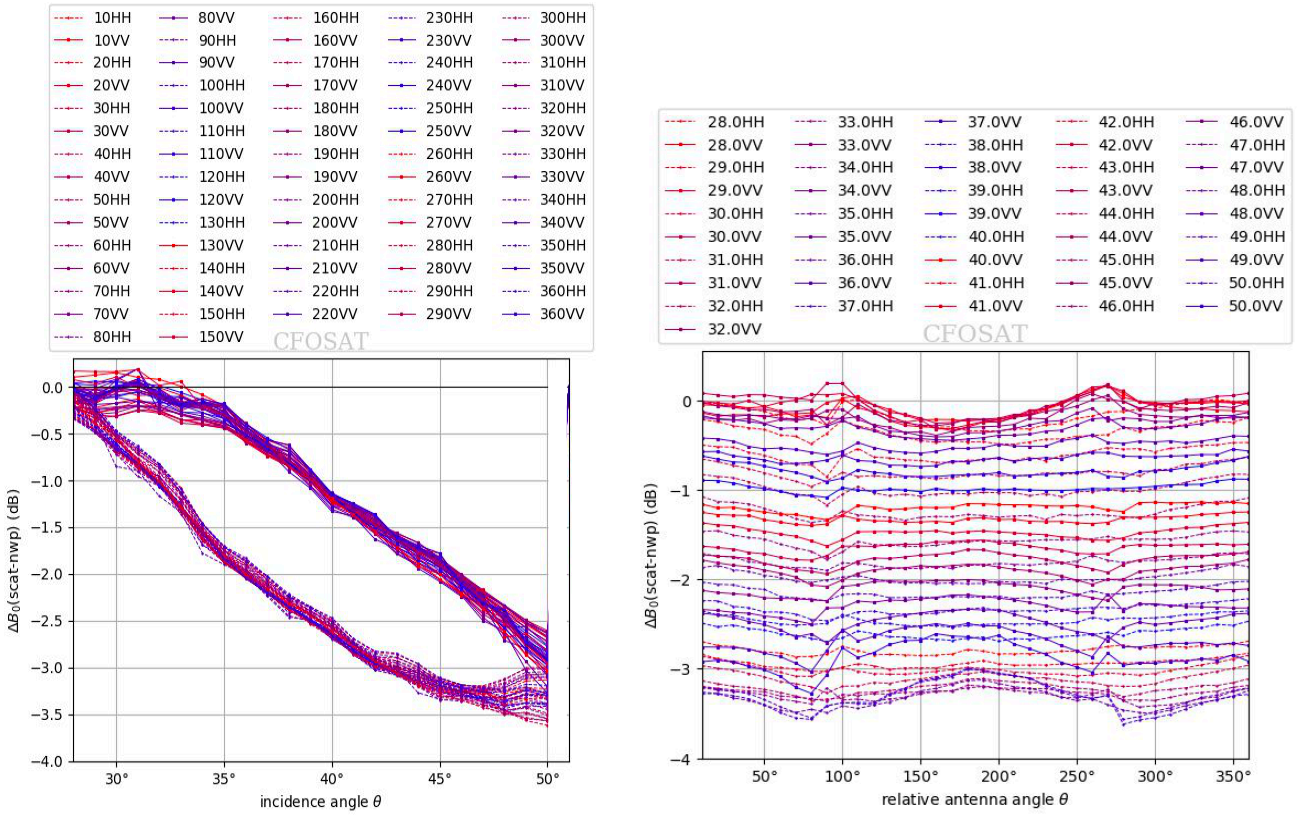

(a) (b)

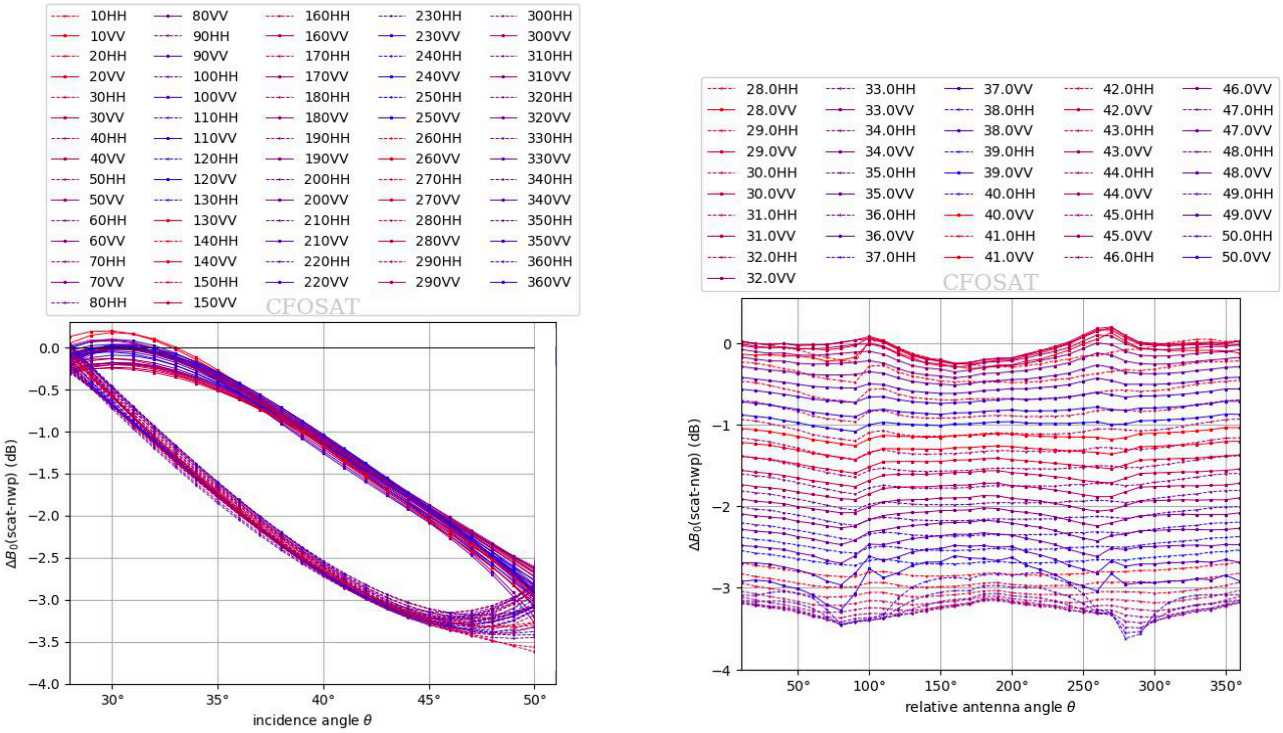

(c) (d)

Figure 15. NOCant for the 25-km product extrapolated at incidence angle bin 50° for the antenna azimuth angle bin 90°, 100°, 270°, and 280°, dash lines are HH polarization, solid lines are VV polarization. (a) NOCant as a function of incidence angle per antenna azimuth angle bin; (b) NOCant as a function of antenna azimuth angle per incidence angle bin; (c) 3rd order polynomial fit of the NOCant as a function of incidence angle per antenna azimuth angle bin; (d) 3rd order polynomial fit of the NOCant as a function of antenna azimuth angle per incidence angle bin.

Note that for NOCinc the NWP wind direction is sampled uniformly for all wind speeds and incidence angles to reduce calibration error [6]. Calibration errors may occur through systematic NWP wind directions errors (Belmonte Rivas and Stoffelen 2019)(Trindade et al. 2020) and the global wind direction PDF variation by a factor of two. The error and PDF variations are very similar for each incidence and beam azimuth angle [6] but interfere differently with the harmonic terms of equation (3) for varying beam azimuth and for varying A_2 in particular for different wind speeds and incidence angle. Hence, the NOCant calibration error may depend on azimuth. Nevertheless, the large backscatter biases need correction before wind retrieval and in next section both NOCinc and NOCant are tested.

4. Wind retrieval performance evaluation

4.1 Comparison of the wind statistics with NOCinc and NOCant corrections

In this section we compare the wind statistics using NOCinc corrections and NOCant corrections. The CWDP (CFOSAT Wind Data Processor ("CWDP," n.d.)) is used to generate 25-km wind products over March 2019.

The Maximum Likelihood Estimator (MLE) as mentioned in section 3 is a measure of how well the measurements and GMF fit to each other and it is an indicator of how well the retrieved wind is represented. For SCAT, the expectation value <MLE> is varying as a function of WVC. The MLE is normalized with a WVC dependent factor, yielding an expectation value of 1, in order to make it easier for monitoring and quality control to check MLE values. A large MLE value means that the measurements in a WVC do not represent the wind well and when the MLE is larger than a certain threshold value, it will be flagged by the quality control (M Portabella and Stoffelen 2002). Because the wind retrievals with NOCinc or with NOCant result in different MLE characteristics, they would result in their own MLE normalization and quality control threshold. However, in order to make the MLEs comparable, the same MLE normalization and quality control threshold are applied with both NOC methods. The resulting MLEs as a function of WVC are shown in Figure 16. In the NOCinc corrected case, only the MLE values located at outer-swath WVCs are lower than NOCant. This might be because at outer WVCs only high incidence angles are used and NOCint uses all azimuth angles to estimate the backscatter bias, while the NOCant bias estimates using only the antenna azimuth angles around 90° and 270° may be less accurate (section 3.1.2), which might cause over or under correction. However, the MLE values of NOCant at the other WVCs are lower than NOCinc especially at the nadir WVCs, which implies that NOCant corrections generally result in backscatter values that better fit the GMF than those using NOCinc corrections.

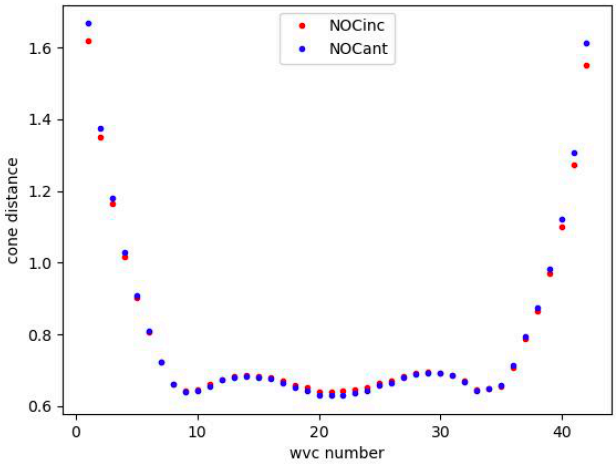

Figure 16. Collocated cone distance as a function of WVC number with the same MLE normalization and quality control threshold (NOCinc is red, NOCant is blue).

Figure 17(a) shows the ECMWF wind speed PDF per WVC and (b) (c) (d) show the retrieved wind speed PDFs per WVC without NOC correction, with NOCinc correction, and with NOCant correction. The wind speed PDF improves significantly with both NOCinc and NOCant corrections and the impact can be seen in the rectangular box (Figure 17 c and d). The peaks of the wind speed PDFs per WVC come closer together with NOCant than with NOCinc for wind speeds between 5m/s and 8m/s. The spread of the wind speed bias for all WVCs becomes narrower for the wind retrieval result with NOCant correction than with NOCinc correction (Figure 18 a and b, rectangular box).

Figure 19 shows the wind speed bias and the standard deviation of the wind speed bias as a function of WVC using NOCinc and NOCant corrections and without NOC with respect to the NWP winds from ECMWF. The wind speed bias and SD show very similar patterns for both correction methods. They show a symmetrical pattern where the outer and nadir WVCs have higher bias and SD, whereas the sweet swath WVCs have the lowest bias and SD. The average wind direction bias is reduced about 43% with NOCant correction as compared to NOCinc correction, whereas the average SD of the wind direction bias is slightly reduced (Figure 20). Even though both NOCinc and NOCant are able to improve the wind direction bias, the shape of the wind direction bias keeps symmetry for NOCant correction, and it shows unbalanced bias at the outer WVCs for NOCinc correction.

The wind direction relative to the satellite motion direction is called relative wind direction here. The 2D bias of the relative wind direction as a function of WVC and relative wind direction is shown in Figure 21. In this evaluation, we are able to see the relative wind direction bias with respect to the satellite track direction at all the WVCs. The nadir swath gives stronger bias as compared to the other parts of the swath. The NOCant correction is better able to reduce the bias in the nadir WVCs than NOCinc correction. As is shown in Figure 21, the bias distribution pattern is quite similar for NOCinc and NOCant, but the NOCant correction yields smaller biases in the nadir WVCs, especially in the rectangular boxes, as compared to the NOCinc correction. The bias is 6.10° for NOCinc and 5.53° for NOCant (black dashed box), whereas it is -6.16° for NOCinc and -5.62° for NOCant (black solid box). For the entire swath, the bias is -0.27° for NOCinc and -0.17° for NOCant. The same phenomenon can be observed in the standard deviation of the relative wind direction bias (Figure 22). The SD is smaller in the nadir swath with NOCant correction as compared to NOCinc correction. This indicates that the ability of NOCant correction for the wind direction bias is better than NOCinc, especially at the nadir WVCs.

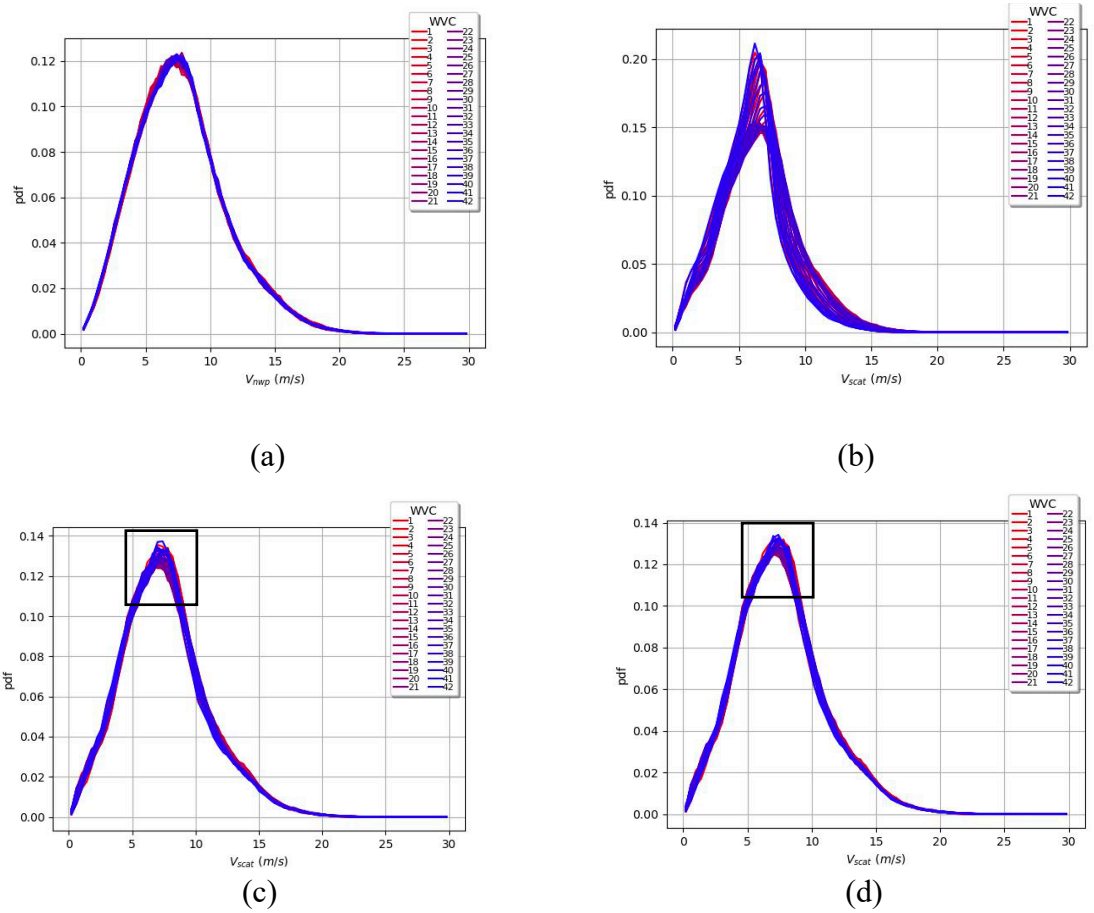

Figure 17. Wind speed PDF per WVC. (a) ECMWF; (b) SCAT without NOC correction; (c) SCAT with NOCinc correction; (d) SCAT with NOCant correction.

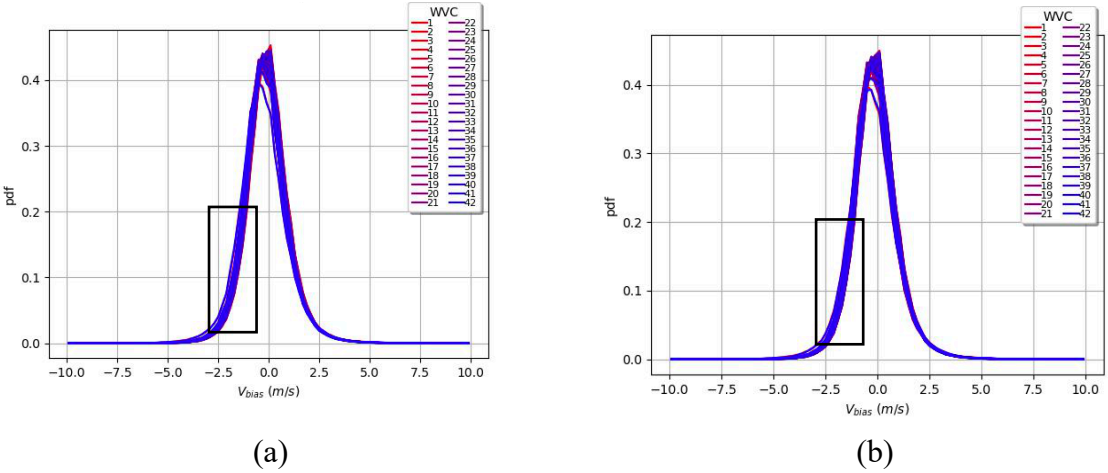

Figure 18. Wind speed difference PDF per WVC. (a) with NOCinc correction; (b) with NOCant correction.

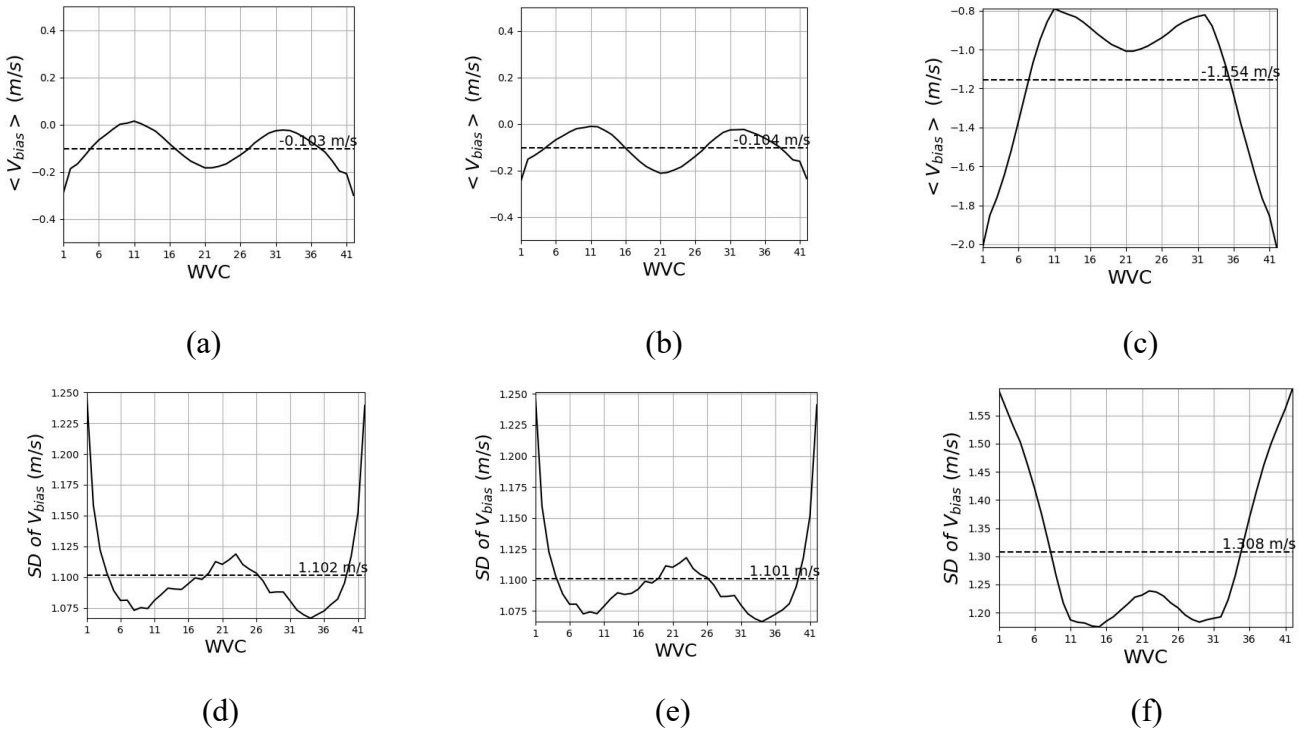

Figure 19. (a) wind speed bias as a function of WVC with NOCinc correction; (b) with NOCant correction; (c) without NOC correction. (d) standard deviation of the wind speed bias as a function of WVC with NOCinc correction; (e) with NOCant correction; (f) without NOC correction.

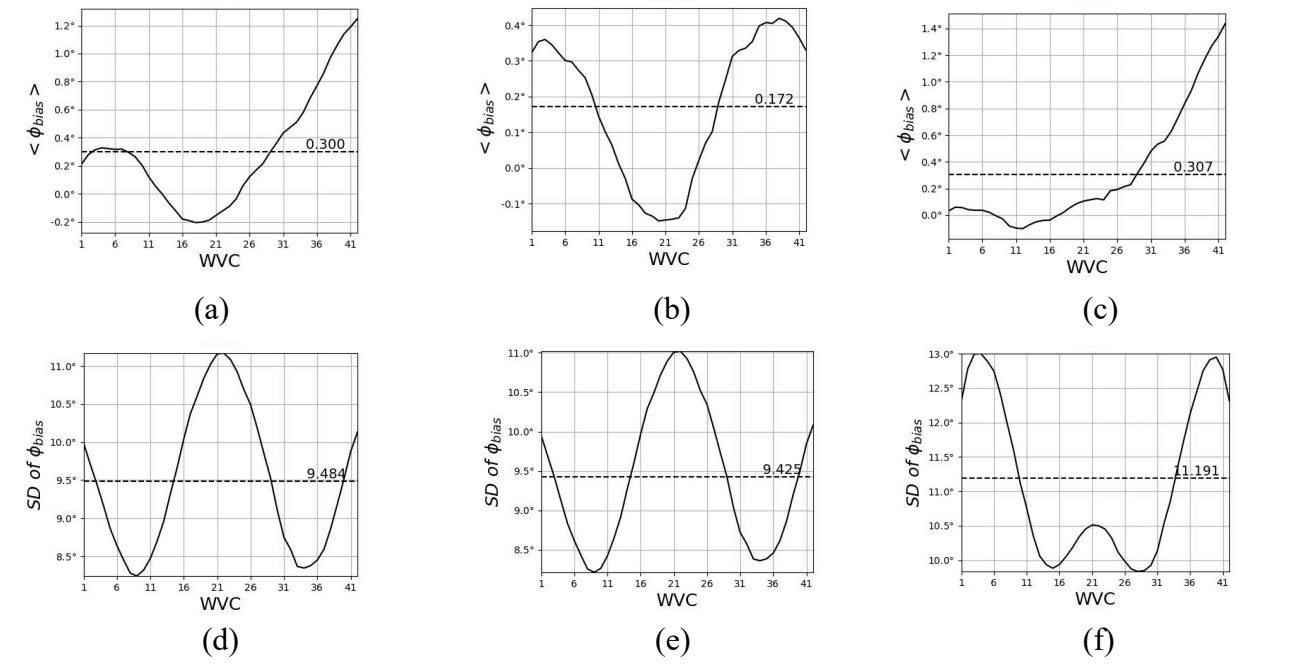

Figure 20. (a) wind direction bias as a function of WVC with NOCinc correction; (b) with NOCant correction; (c) without NOC correction. (d) standard deviation of the wind direction bias as a

function of WVC with NOCinc correction; (e with NOCant correction; (f) without NOC correction.

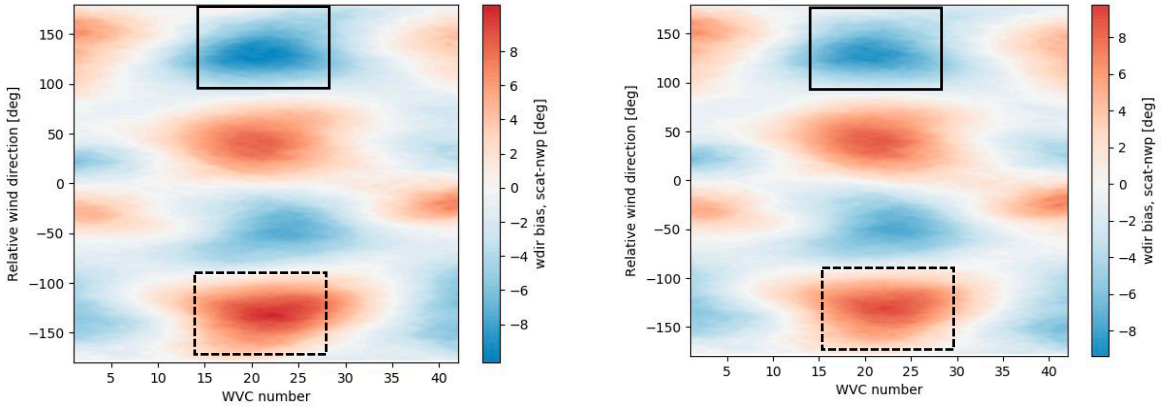

(a) (b)

Figure 21. Relative wind direction bias (relative to the satellite motion direction) per WVC. (a) with NOCinc correction. (b) with NOCant correction.

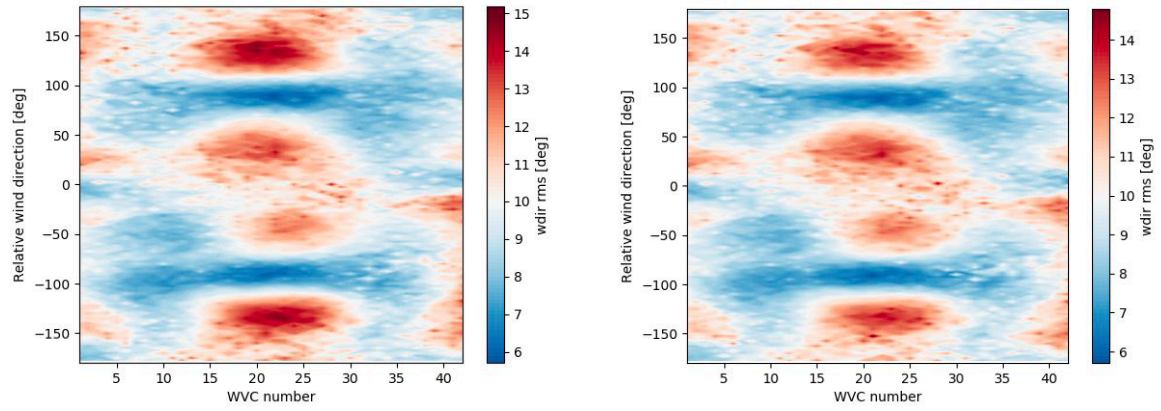

(a) (b)

Figure 22. Standard deviation of relative wind direction (relative to the satellite motion direction) bias per WVC. (a) with NOCinc correction. (b) with NOCant correction.

4.2 Wind retrieval performance across the swath with NOCant

Wind retrieval with NOCant is chosen to analyze the wind retrieval performance across the swath because it somewhat improves the wind retrieval quality as compared to NOCinc according to the analysis in section 4.1. The contoured histograms in Figure 23 and Figure 24 provide the statistics of the wind speed, wind direction with respect to a wind blowing from the north, and wind components *u* eastward and *v* northward versus the ECMWF model winds.

The wind speeds are off the diagonal without NOC correction and the wind directions contain many spurious directions perpendicular to the true value in the plot, especially below the diagonal (Figure 23a) and NOCant correction corrects the wind speed deviations from the diagonal and also effectively removes many false directions (Figure 23b).

Due to the rotating instrument configuration, the wind retrieval quality is varying across the swath. In general, sweet WVCs contain the most diverse geometries as well as the largest number of views, which leads to a better wind retrieval. The azimuth view angles are mainly around 0° or 180° in the nadir WVCs, and the number of views is smaller, while nadir WVCs contain diverse incidence angles. The worst wind retrieval occurs in the outer-swath WVCs, where the azimuth angles are limited around 90° and 270°, only high incidence angles occur, and the number of views is the smallest. As shown in Figure 24, the wind speed collocation statistics stay quite similar for the WVCs at nadir, sweet and outer swath. The narrowest spread of the wind speed histogram is in the sweet WVCs, and the widest in the outer WVCs. Wind speeds above 20m/s for both nadir and outer WVCs tends to be higher as compared to the ECMWF model speed, whereas in the sweet WVCs it remains close to the diagonal (Figure 24, red points at the diagonal of the wind speed histogram). The shape of the nadir wind direction histogram (Figure 24a) is an oscillating curve. The spurious wind directions, which are perpendicular to the true values, do not appear in the nadir WVCs, but appear mainly in the outer WVCs and to some extent in the sweet WVCs (Figure 24 b and c). The ambiguous wind directions are mainly caused by nadir and outer WVCs. The oscillating shape of the wind direction histogram cannot be fully corrected by the NOCant correction, even though NOCant improves the wind direction at nadir WVCs as stated in section 4.1.

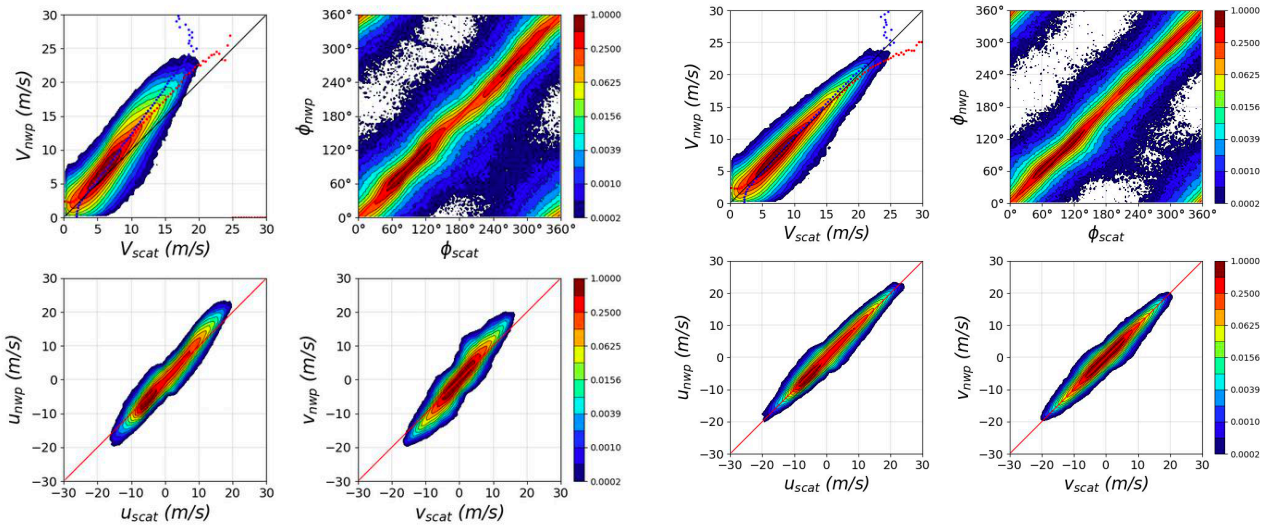

(a) (b)

Figure 23. Contoured wind speed, wind direction (all wind speeds and wind directions are included), u/v components histogram of SCAT-retrieved 2DVAR selected solution (20190301-20190331) : (a) without NOC; (b) with NOCant.

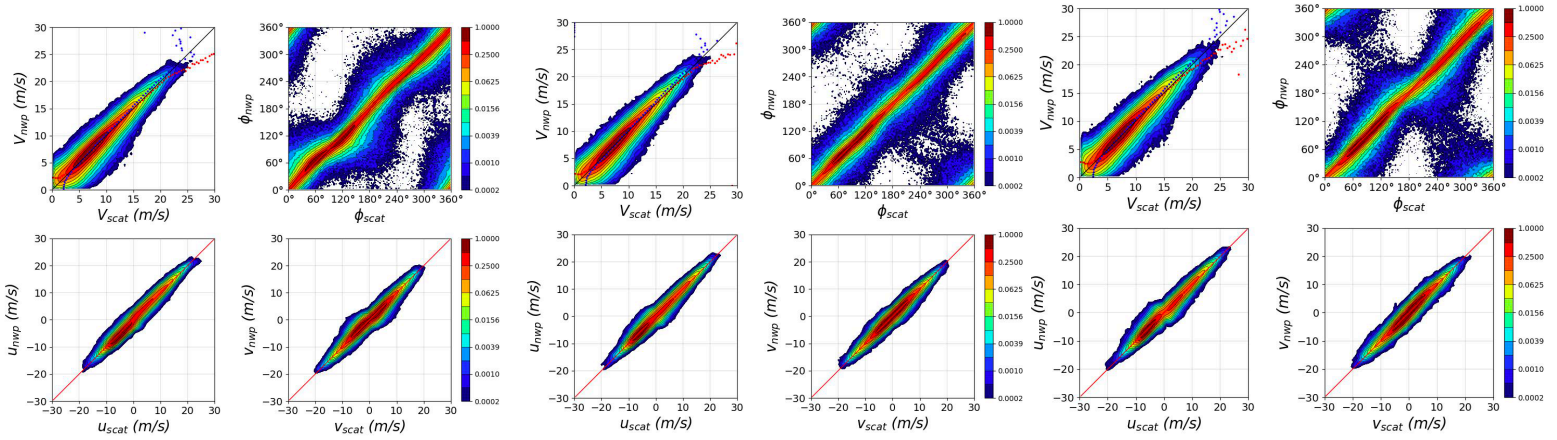

(a) (b) (c)

Figure 24. Contoured wind speed, wind direction (all wind speeds and wind directions are included), u/v components histograms of SCAT-retrieved 2DVAR selected solution with NOCant (20190301-20190331) at: (a) nadir swath (WVC number from 12 to 30); (b) sweet swath (WVC number from 6 to 11 and 31 to 37); (c) outer swath (WVC number from 1 to 5 and 38 to 42).

5. Discussion and conclusion

The analysis of the characteristics of the CFOSAT Level-2A data shows that the unique design of the rotating fan-beam instrument leads to a varying geometry across the swath and this feature yields different wind retrieval performance across the swath as well. The WVCs are classified into three groups: outer WVCs (number 1-5, number 38-42); sweet WVCs (number 6-12, number 31-37); nadir WVCs (number 13-30). The sweet WVCs provide the most favorable and diverse geometries for wind retrieval, while the outer and nadir WVCs both have their own limitations. Among both the unfavorable outer and nadir WVCs, the diversity of the azimuth angle is limited, the number of views is much less than in the sweet WVCs, while nadir WVCs contain a large range of incidence angles and more views than outer WVCs. The average wind speed bias, SD (Figure 19 b and e) and the average wind direction bias are lower in the nadir WVCs than in the outer WVCs (Figure 20 b), whereas the wind direction SD stays almost the same (Figure 20 d). This indicates that the increased number of views with a large of range incidence angles in the nadir WVCs improves the wind retrieval quality as compared to the outer WVCs.

If we compare the relative wind direction bias with respect to the satellite motion direction (Figure 21), we can see that the relative wind direction bias in the nadir WVCs is higher than in the outer WVCs, and if the wind direction bias is averaged over all the relative wind directions, a small value of the bias remains, as can be seen in Figure 20 b. As shown in Figure 24 (a and c), the oscillating shape of the wind direction in the nadir WVCs is more obvious than in the outer WVCs, while in the outer WVCs there are spurious wind directions perpendicular to the diagonal. This oscillating shape can be related to Figure 21, which shows that the most pronounced positive

and negative relative wind direction bias and SD are in the nadir WVCs. These effects are less pronounced for the outer WVCs and least obvious for sweet WVCs. The azimuth angle range in the outer WVCs is a bit larger than in the nadir WVCs (Figure 6) which leads to a bit more scattered location of the slices (Figure 5), but the number of slices and views in the outer WVCs are less than in the nadir WVCs. Even though both regions have their own limitations, the combination of these features leads to more diagonal retrieved wind direction bias in the outer WVCs, but with more ambiguous wind directions away from the diagonal.

NWP Ocean Calibration (NOC) is an effective and established way to correct measured σ°s before wind retrieval. In order to adapt to the rotating antenna design of the SCAT instrument, NOCant (NOC as a function of incidence angle and antenna azimuth angle) is proposed here and it is also compared with the classic NOCinc (NOC as a function of incidence angle), which has been successfully implemented already on various other scatterometers. The comparison shows that the NOCant correction results in backscatter values that generally fit better to the GMF than the NOCinc correction, while for outer WVCs the limited azimuth range around 90° and 270° (for only high incidence angle), appears to lead to an over or under correction of the σ°s. It may be worthwhile to relax to NOCinc corrections for the σ°s with high incidence angles and apply NOCant on the other σ°s in order to reduce the detrimental effect of NOCant in the outer swath, though this may compromise the sweet swath performance. The wind speed PDFs per WVC are more uniform with NOCant than with NOCinc (Figure 17 c and d, Figure 18), whereas the average wind speed bias across the WVCs is similar for both methods (Figure 19). NOCant gives more pronounced improvements in the wind directions. The average wind direction bias is reduced with about 43% (Figure 20 a and b). Moreover, NOCant makes the shape of the wind direction bias across the swath more symmetric. If we decompose the relative wind direction bias as a function of WVC and relative wind direction (Figure 21), as we discussed above, the strongest bias appears at nadir WVCs and NOCant is able to reduce this bias more effectively than NOCinc. However, the bias in the outer and sweet WVCs stays more or less the same for both NOC corrections. Nadir WVCs have limited azimuth diversity which makes the wind retrieval sensitive to backscatter biases. Hence, the key parameters for NOCant, azimuth angle and incidence angle, make NOCant more effective on nadir WVCs than on outer WVCs. The diversity at sweet WVCs is very good and hence the sensitivity to backscatter calibration effects more limited.

In conclusion, the characteristics of the CFOSAT SCAT level-2A data are analyzed in this paper and the wind retrieval performance strongly depends on the location across the swath. NOCant is developed to adapt to the rotation angle of the fan-beam of the SCAT. NOCant and NOCinc corrections are compared, where NOCant corrections makes the σ°s generally fit better to the GMF than NOCinc, except for the outer WVCs. NOCant also largely improves the ECMWF wind direction bias, as compared to NOCinc, especially at nadir WVCs. For the future study, it might be possible to combine NOCant and NOCinc in a way to eliminate the over correction of the NOCant at the outer WVCs and possibly keep the advantages of NOCant at the other WVCs.

Acknowledgements

We acknowledge the support of the CFOSAT team, CNES and NSOAS in providing the data, status and mission information. We thank Wenming Lin (NUIST) and Yun Richeng (NSSC) for providing the necessary technical information to carry out our work. The support from the EUMETSAT Ocean and Sea Ice Satellite Application Facility is further much appreciated.
Data for this research are not publicly available because the data for this project are accessable within the members in the project frame and currently it can be accessed through requesting for the other parties. For meeting FAIR requirements, data archiving is underway and the repository is in discussion with the data providers of CNES and NSOAS, which will be accessible by acceptance of the paper.

References

Belmonte Rivas, Maria, and Ad Stoffelen. 2019. "Characterizing ERA-Interim and ERA5 Surface Wind Biases Using ASCAT." *Ocean Science* 15 (3). https://doi.org/10.5194/os-15-831-2019.

Chi, Chong Yung, and Fuk K. Li. 1988. "A Comparative Study of Several Wind Estimation Algorithms for Spaceborne Scatterometers." *IEEE Transactions on Geoscience and Remote Sensing* 26 (2): 115–21. https://doi.org/10.1109/36.3011.

"CWDP." n.d. https://nwp-saf.eumetsat.int/site/software/scatterometer/cwdp/.

Dunbar, R Scott, S Vincent Hsiao, Young-joon Kim, Kyung S Pak, Barry H Weiss, and Angela Zhang. 2001. "Science Algorithm Specification for SeaWinds on QuikSCAT and SeaWinds on ADEOS-II." *Jet Propulsion*. California, US.

Freilich, Michael H., Hongbo Qi, and R. Scott Dunbar. 1999. "Scatterometer Beam Balancing Using Open-Ocean Backscatter Measurements." *Journal of Atmospheric and Oceanic Technology* 16 (2): 283–97. https://doi.org/10.1175/1520-0426(1999)016<0283:SBBUOO>2.0.CO;2.

Gelsthorpe, R V, E Schied, and J J W Wilson. 2000. "ASCAT - Metop's Advanced Scatterometer." *ESA BULLETIN-EUROPEAN SPACE AGENCY*.

Kloe, Jos De, Ad Stoffelen, and Anton Verhoef. 2017. "Improved Use of Scatterometer Measurements by Using Stress-Equivalent Reference Winds." *IEEE Journal of Selected Topics in Applied Earth Observations and Remote Sensing* 10 (5). https://doi.org/10.1109/JSTARS.2017.2685242.

Li, Zhen, Ad Stoffelen, and Anton Verhoef. 2019. "A Generalized Simulation Capability for Rotating Beam Scatterometers." *Atmospheric Measurement Techniques* 12: 3573–94. https://doi.org/10.5194/amt-2018-232.

Lin, Chung-Chi, B Rommen, J J W Wilson, F Impagnatiello, and P S Park. 2000. "An Analysis of a Rotating, Range-Gated, Fanbeam Spaceborne Scatterometer Concept." *Geoscience and Remote Sensing, IEEE Transactions On*. https://doi.org/10.1109/36.868870.

Pierson, W. J. 1989. "Probabilities and Statistics for Backscatter Estimates Obtained by a Scatterometer." *Journal of Geophysical Research*. https://doi.org/10.1029/JC094iC07p09743.

Portabella, M, and A Stoffelen. 2002. "Characterization of Residual Information for SeaWinds Quality Control." *IEEE Trans. Geosci. Rem. Sens* 40 (12): 2747–59.

Portabella, Marcos, and Ad Stoffelen. 2004. "A Probabilistic Approach for SeaWinds Data Assimilation." *Quart. J. R. Met. Soc.* 130 (596): 127–52.

SCAT-DP team. 2010. “Oceansat-2 Scatterometer Algorithms for Sigma-0, Processing and Products Format.” India.

Snyder, John P. 1982. “Map Projections Used by the U.S. Geological Survey.”

Stoffelen, Ad, and David Anderson. 1997. “Scatterometer Data Interpretation: Measurement Space and Inversion.” *Journal of Atmospheric and Oceanic Technology* 14: 1298–1313. https://doi.org/10.1175/1520-0426(1997)014<1298:SDIMSA>2.0.CO;2.

Stofflen, Ad. 1999. “A Simple Method for Calibration of a Scatterometer over the Ocean.” *Journal of Atmospheric and Oceanic Technology*, no. February: 275–82. https://doi.org/10.1175/1520-0426(1999)016<0275.

Trindade, Ana, Marcos Portabella, Ad Stoffelen, Wenming Lin, and Anton Verhoef. 2020. “ERAstar: A High-Resolution Ocean Forcing Product.” *IEEE Transactions on Geoscience and Remote Sensing* 58 (2). https://doi.org/10.1109/TGRS.2019.2946019.

Verhoef, Anton. n.d. “PenWP Software.” KNMI. Accessed January 10, 2020. http://projects.knmi.nl/scatterometer/nwpsaf/.

Verspeek, Jeroen, Ad Stoffelen, Anton Verhoef, and Marcos Portabella. 2012. “Improved ASCAT Wind Retrieval Using NWP Ocean Calibration.” *IEEE Transactions on Geoscience and Remote Sensing* 50 (7): 2488–94. https://doi.org/10.1109/TGRS.2011.2180730.

Vogelzang, Jur. 2013. “Two-Dimensional Variational Ambiguity Removal (2DVAR).” de Bilt, the Netherlands.

Vogelzang, Jur, and Ad Stoffelen. 2018. “Improvements in Ku-Band Scatterometer Wind Ambiguity Removal Using ASCAT-Based Empirical Background Error Correlations.” *Quarterly Journal of the Royal Meteorological Society* 144 (716). https://doi.org/10.1002/qj.3349.

Wang, Zhixiong, Ad Stoffelen, Chaofang Zhao, Jur Vogelzang, Anton Verhoef, Jeroen Verspeek, Mingsen Lin, and Ge Chen. 2017. “An SST-Dependent Ku-Band Geophysical Model Function for RapidScat.” *Journal of Geophysical Research: Oceans* 122 (4): 3461–80. https://doi.org/10.1002/2016JC012619.

Wentx, Frank J., and Deborah K. Smith. 1999. “A Model Function for the Ocean Normalized Cross Section at 14 GHz Derived from NSCAT Observations.” *Journal of Geophysical Research* 104 (C5): 11499–514.

Wentz, Frank J, S. Peteherych, and L. A. Tomas. 1984. “A Model Function for Ocean Radar Cross Sections at 14.6 GHz.” *Journal of Geophysical Research* 89 (C3): 3689–3704.

Yun, Risheng, Ad Stofflen, Jeroen Verspeek, and Anton Verhoef. 2012. “NWP Ocean Calibration of Ku-Band Scatterometers.” In *IEEE International Geoscience and Remote Sensing Symposium*. Munich, Germany. https://doi.org/10.1109/IGARSS.2012.6350970.